Supporting Information

Energy Landscape of Zirconia Phase Transitions

Shu-Hui Guan, Xiao-Jie Zhang, Zhi-Pan Liu*

Collaborative Innovation Center of Chemistry for Energy Material, Key Laboratory of Computational Physical Science (Ministry of Education), Shanghai Key Laboratory of Molecular Catalysis and Innovative Materials, Department of Chemistry, Fudan University, Shanghai 200433, China

Part 1 The orientation relation and habit plane suggested in literatures

Table SI The orientation relation (OR) for t-m phase transition of ZrO_2 in literatures. In this table, the conventional cell of tetragonal phase is utilized for the notation of surface and direction. HP: the habit plane

Reference	OR of t-m transformation	Material and method
Bailey[1] 1964	$(100)_m//(110)_t;[001]_m//[001]_t$ $(100)_m//(001)_t;[001]_m//[110]_t$ $(100)_m//(110)_t;[001]_m//[110]_t$	thin films of zirconia; TEM
Wolten[2] 1964	$(101)_m//(111)_t;[010]_m//[110]_t$ $(101)m//(100)_t;[010]_m//[001]_t$	High temperature, single crystal; XRD
Smith[3] 1965	$(100)_m//(110)_t;[001]_m//[001]_t$	synthetic single crystal; XRD
Patil[4] 1970	$(100)_m//(110)_t;[010]_m//[001]_t$	high temperature; XRD
Bansal and Heuer[5] 1974	>1000℃ $(100)_m//(110)_t;[010]_m//[001]_t$, <1000℃ $(100)_m//(110)_t$;$[001]_m//[001]_t$ HP $(100)_m$	Single crystal; TEM
Buljan[6] 1976	$(001)_m//(001)_t;[100]_m//[110]_t$,HP $(001)_m$ $(100)_m//(110)_t;[001]_m//[001]_t$,HP $(100)_m$	Single crystal; TEM, XRD
Muddle and Hannink[7] 1986	$(001)_m//(110)_t;[100]_m//[110]_t$,HP $(671)_m$,$(761)_m$ $(100)_m//(110)_t;[001]_m//[110]_t$,HP~$(100)_m$ $(100)_m//(110)_t;[001]_m//[001]_t$,HP~$(010)_m$	MgO-partially stabilized zirconia; TEM and electron micro-diffraction
Chien et al. [8] 1988	$(100)_m//(110)_t;[010]_m//[001]_t$	3Y-ZrO_2; Raman, TEM
Hayakawa et al. [9] 1989	$(100)_m//(100)_t;[001]_m//<100>_t$,HP~$(-301)_m$	2mol%Y_2O_3-ZrO_2; XRD, EM
Hugo and Muddle[10] 1990	$(100)_m//(-110)_t$; $[001]_m//[110]_t$ $(001)_m//(110)_t$; $[100]_m//[-110]_t$ $(100)_m//(-110)_t;[001]_m//[001]_t$	12mol%CeO_2-zirconia; Electron diffraction
Zhu[11] 1996	$(001)_m//(110)_t$; $[1\text{-}10]_m//[100]_t$,HP$(671)_m$ $(111)_m=(01\text{-}1)_t$	3mol%Y_2O_3-ZrO_2; HRTEM
Shevchenko; Madison and Glushkova[12] 2001	$(100)_m//(110)_t;[001]_m//[001]_t$	Nanosized zirconia centaur particles; Theoretical modelling
Shevchenko; Khasanov and Madison[13] 2002	$(111)_m//(101)_t$,HP$(111)_m=(101)_t$	Zirconia nanoparticles; HRTEM
Kasatkin et al[14] 2004	$(100)_m$ $//(110)_t;[001]_m//[001]_t$;(1) $(013)_m$ $//(116)_t;[001]_m//[001]_t$;(2) $(100)_m$ $//(001)_t;[001]_m//[110]_t$;(3) $(011)_m//(100)_t;[100]_m//[001]_t$;(4)	CuO/ZrO_2; HRTEM

Wu et al[15] 2011	$(100)_m//(110)_t$;$[010]_m//[001]_t$ $(100)_m//(110)_t$; $[001]_m//[001]_t$	Hot-pressed sintered 3YSZ ceramics with different content of TiN; XRD, SEM, TEM
Chiao and Chen[16] 1990	$(100)_o//(100)_m$;$[010]_o/[010]_m$ $(010)_o//(001)_t$;$[100]_o//[100]_t$ o(*Pbca*, n^o 61)	submicroZrO_2 particles in the Nb matrices; *In situ* TEM
Simeone[17] 2003	$(100)_m//(110)_t$;$[010]_m//[001]_t$ o(*Pbcn* n^o 60)	High-purityZrO_2 powder (99.2%); neutron diffraction, Landau theory
Trolliard[18] 2011	$(100)_m//(110)_t$;$[001]_m//[001]_t$ $(001)_t//(010)_o$; $[110]_t//[100]_o$ o-phase (*Pbc1/2*, n^o 29)	Phenomenological Theory, the group theory

Liu et al. [19]
2014
	$(100)_t//(100)_{oA}//(011)_{oB}$;$[001]_t//[010]_{oA}//[100]_{oB}$
	oA(*Pbcm,* n^o 57; *Pbc1/2* n^o 29);
	oB(*Pbca,* n^o 61)
		ZrO_2 NPs;
		HRTEM

Part 2 Theoretical methods

a. Stochastic Surface Walking (SSW) pathway sampling

The SSW methodology has been described in our previous work in detail[20-21]. We have showed that the SSW method is able to explore the potential energy surface (PES) to identify unexpected new structures, including clusters and crystals, and at the mean time to collect the reaction pathways leading to them. This is attributed to the fact that SSW PES searching involves generally small displacement on lattice and atoms, and thus the pathway information is maintained from one minimum to another.

The purpose of SSW crystal pathway sampling is to establish a one-to-one correspondence for lattice ($L(e_1,e_2,e_3)$, e_i being the lattice vector) and atom (q_i, i=1,..3N, N is the number of atom in cell) from one phase to another. The lattice here does not necessarily be the conventional Bravais lattice but any possible set of lattice that describe the same crystal phase. Using such a pair of coordinates, $Q_{IS}(L,q)$ and $Q_{FS}(L,q)$ (IS and FS are the initial and the final states), it is then possible to utilize double-ended transition state searching method to identify the reaction pathway and the transition state. The current approach is different from the traditional Landau-type theory where the lattice correspondence needs to be assumed. The procedure is described below briefly.

Pathway collection In SSW pathway sampling, firstly, we start from one single phase (starting phase), and utilize the SSW method to explore all the likely phases nearby the phase. A structure selection module is utilized to decide whether to accept/refuse once a new minimum is reached. If the new phase different from the starting phase is identified by the SSW crystal method[22], we record/output the IS (i.e. starting phase) and the FS (a new phase) of the current SSW step. Then, the program will return back to the IS by rejecting the new minimum to continue the phase exploration; On the other hand, if the new minimum identified by SSW is still the starting phase (e.g. the same symmetry but a permutation isomer with varied lattice), the program will accept the new isomeric phase and start the phase exploration from this phase. We repeat this procedure until a certain number of IS/FS pairs are reached.

Pathway screening Secondly, we utilize the variable-cell double-ended surface walking (DESW) method[23] to establish the pseudopathway connecting IS to FS for all IS/FS pairs [24-25]. The approximate barrier is obtained according to DESW pseudopathway, where the maximum energy point along the pathway is generally a good estimate for the true TS [23]. By sorting the approximate barrier height, we can obtain the candidates for lowest energy pathways.

It might be mentioned that at this stage, we generally examined thoroughly all the pathways we identified. Basically, even before we locate exactly the TS, we can have the following important information, including the approximate barrier, the pattern of lattice and atom movement from IS to FS, the habit plane and the OR for the pathways, From these, we can safely rule out the similar pathways and focus on the selected, distinct and low energy pathways.

Lowest energy pathway determination Thirdly, the candidate lowest energy pathways are selected to locate exactly the "true" TS by using DESW TS-search method[23]. By sorting the exact barrier calculated, the energy difference between the TS and the IS, the lowest energy pathways can be finally obtained. All the lowest energy pathways will be further confirmed by extrapolating TS towards IS and FS, and the TSs are validated by phonon spectrum calculation, showing one and only one imaginary mode.

In this work, for t-m phase transition, starting either from tetragonal or monoclinic phases, the SSW simulation in the 12-atom sampling visits 1129 minima nearby IS (see, for example, the possible minima on PES in Figure S1 below) and collects 144 IS/FS pairs (also see Figure S2 below) under the first principles calculation framework; in the 24-atom sampling 1514 minima are visited nearby IS and 125 IS/FS pairs are collected.

Figure S1 plots the configuration energy spectrum (a 0~0.8 eV/f.u. window) of possible ZrO_2 crystal phases (12 atom per cell, i.e. Zr_4O_8). The dataset is taken from 699 minima collected from SSW structure searching. It demonstrates the ability of SSW method for PES exploration. We can see that all common phases, including the monoclinic (M, the global minimum), the tetragonal (T), the cubic (C), and other high pressure forms, such as OII and O (important phase in t-m transition as revealed in this work) have all been identified together with many other isomeric crystal forms.

Figure S2 plots the peudopathways we connected for t-m phase transitions. It includes the results from both 12-atom and 24-atom sampling. In the 12-atom sampling, 79 of 144 pathways have the approximate barrier below 200 meV/f.u. with respect to m-phase. 10 lowest energy pathways in the bottom left corner are selected for the exact TS location. This leads to the finding of the **Path I**, **II**, **III**, **IV** (see Figure S3). In the 24-atom sampling, 14 of 125 pathways have the approximate barrier below 200 meV/f.u with respect to m-phase. 9 lowest energy pathways in the bottom left corner are selected for the exact TS location. This leads to the finding of the three lowest pathways (**Path I**, **II** and **III**) already identified from 12-atom sampling and a new higher energy path, **Path V** (via OI, see below for description and Figure S3).

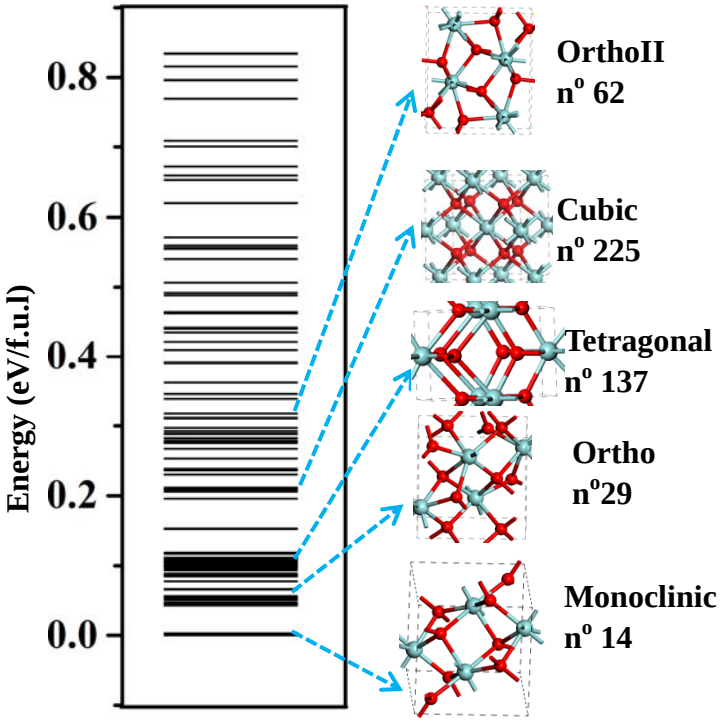

FIG. S1. The configuration energy spectrum of the ZrO_2 crystal structure obtained from SSW crystal global structure search. Zr atom: Cyan: O atom: Red

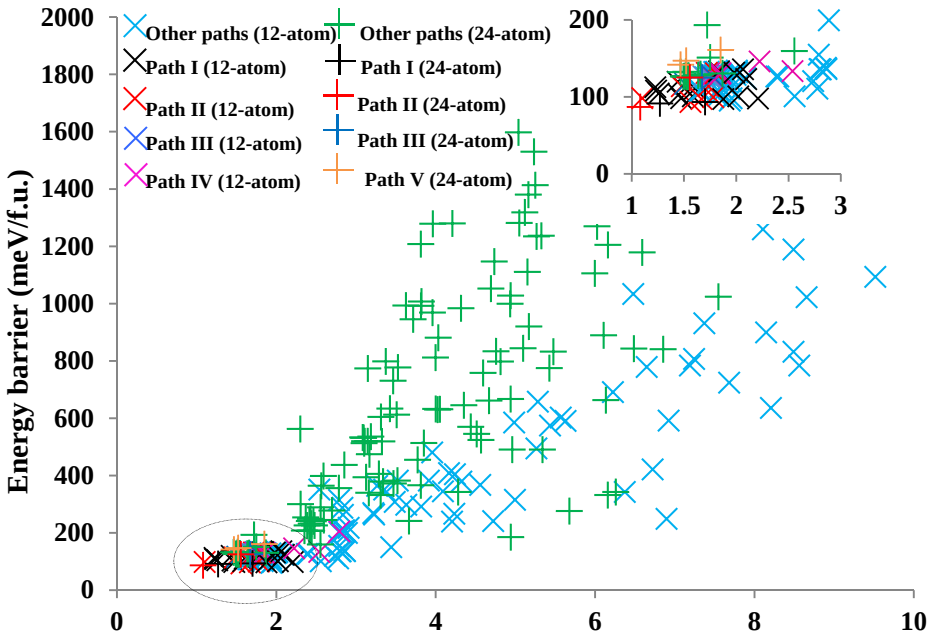

Figure S2 Pathway screening by plotting approximate energy barrier per ZrO_2 formula (meV/f.u. with respect to m-phase) versus a scaled Euclidean distance (Å) between two phases (measured from the pathways). In total, there are 144 pathways from 12-atom sampling and 125 pathways from 24-atom sampling. The approximate barrier is obtained according to DESW pseudopathway, where the maximum energy point along the pathway is generally a good estimate for the true TS [23]. Of those 144 pathways from 12-atom sampling, 79 pathways have the approximate barrier below 200 meV/f.u with respect to m-phase. We select 10 lowest energy pathways in the bottom left corner and utilize DESW TS search method to identify the exact TS. This leads to the finding of the **Path I**, **II**, **III** and **IV**. Of those 125 pathways from 24-atom sampling, 14 pathways have the approximate barrier below 200 meV/f.u with respect to m-phase. We select 9 lowest energy pathways in the bottom left corner and utilize DESW TS search method to identify the exact TS. This leads to the finding of **Path I**, **II**, **III** and **V** (via OI).

Supercell size effect

In this work, we carried out first principles DFT SSW pathway sampling in 12-atom and 24-atom supercell and the empirical potential SSW pathway sampling in 48-atom supercell.

By comparing the 12-atom and 24-atom sampling, we found that **Path I**, **II** and **III** are identified in both simulations and remain to be the lowest energy pathways. This is not surprising considering that the calculated barrier of the two lowest pathways (**Path I** and **II**) from t-phase to m-phase are already extremely low, being ~3 meV. On the other hand, the fact that the simulation using two different supercells produces the same lowest energy pathways implies that the atoms in ZrO_2 t-m phase transition are diffusionless, obeying the nature of diffusionless Martensitic phase transition (we note that the lowest energy pathway contains only 6-atom per cell for alpha-to-omega phase transition of Ti according to the previous theoretical work by Trinkle [26]).

Path V is a pathway being identified only in 24-atom sampling, which involves the intermediate phase OI (n^o 61， Pbca), a known high pressure phase of ZrO_2. OI phase contains 24 atoms per primitive cell (thus not seen in 12-atom sampling) and it was considered as a possible intermediate for t-m phase transition previously [27]. The crystal structure of OI is very similar to the o-phase (n^o 29, Pbc1/2) identified in this work and also proposed previously[28]. Trolliard et al[29] suggested that OI might be formed by doubling the ***a*** lattice parameter of o-phase, originated from the ordering of stacking faults in the o-phase. According to our pathway sampling with 24 atoms, there is a direct pathway from the o-phase to OI phase, but it has a very high barrier, 81.1 meV/f.u. with respect to o-phase (see Figure S3). Because **Path V** (indirect pathway via the OI phase) has an overall much higher barrier compared to the direct pathway from o-phase to m-phase, we consider **Path V** is unlikely to occur kinetically.

We have also attempted to carry out first principles DFT SSW pathway sampling with even larger size supercell, i.e. 48 atom per supercell. We found that DFT calculations are not efficient enough to collect

enough pathway data from SSW sampling. We therefore tested the SSW pathway sampling based on empirical potential[30], which yields 1123 reaction pathways for t-m phase transition. We selected 18 lowest energy pathways and then utilized DFT calculation to verify the reaction path by identifying exactly the TS. This leads to the finding of **Path I** (4 out of 18 pathways). No **Path II** and **III** are identified from the empirical potential SSW sampling. This implies that DFT pathway sampling is more robust and essential to capture all the important pathways for t-m phase transition.

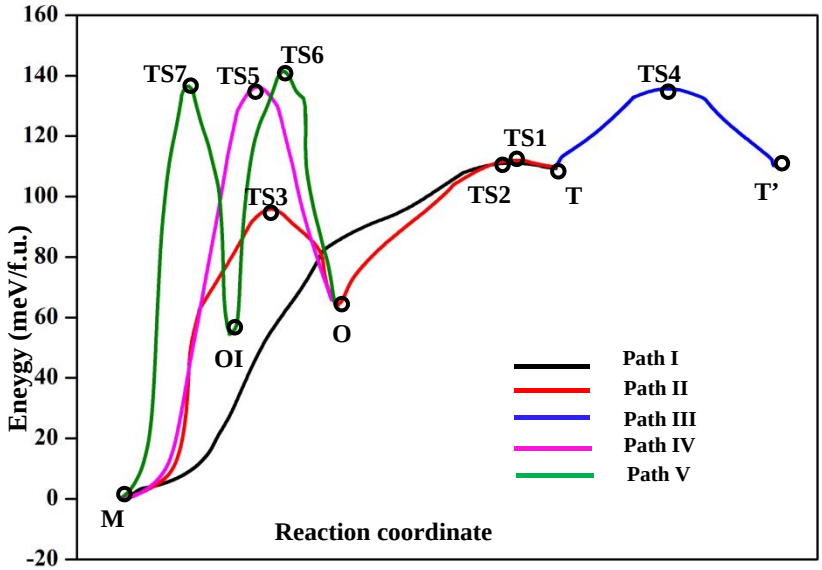

FIG. S3. Potential energy profile including the less favored **Path IV** and **Path V**. Black: **Path I**; Red: **Path II**; Blue: **Path III**; Pink: **Path IV**; Green: **Path V**. T and T': tetragonal ZrO_2; O: orthorhombic ZrO_2; M: monoclinic ZrO_2

TABLE SII. The relative energetics (meV/f.u.) of the key states in **Path I**, **II** and **III** using different DFT functionals and k-point mesh. The energy of m-phase is set as reference.

Functionals	PBE	PBE	PBE	HSE06	HSE06
k-point mesh	4x4x4	6x6x6	8x8x8	4x4x4	6x6x6
m-phase	0.0	0.0	0.0	0.0	0.0
o-phase	66.2	66.3	66.3	56.7	58.1
t-phase	110.6	110.7	110.7	99.6	101.0
TS1	113.1	**113.2**	113.2	110.3	**111.6**
TS2	114.1	**114.1**	114.1	110.4	**111.7**
TS3	98.4	98.4	98.4	104.5	105.2
TS4	139.7	139.9	139.9	125.1	127.2

b. DFT Calculation details

All phase transition pathways are initially sampled using SIESTA package[31] with optimized numerical double-ζ polarization basis set[32] at the GGA-PBE exchange-correlation functional level[33]. The energy cutoff for the real space grid used to represent the density was set as 150 Ry. An energy shift of 0.01 eV was used to determine the orbital-confining cutoff radii. In SSW sampling, the **k**-point mesh utilized was Monkhorst-Pack (4×4×4) set, which is verified to be enough to distinguish low energy pathways.

To obtain accurate energetics for the lowest energy pathways, the plane wave DFT program, Vienna ab initio simulation package VASP [34-35], was utilized, where electron-ion interaction was represented by the projector augmented wave (PAW)[36] and the exchange-correlation functional utilized was GGA-PBE. A plane-wave energy cutoff of 500eV was used. The reference configurations for valence electrons were $4s^2$ $4p^6$ $5s^2$ $4d^2$ for Zr and $2s^2$ $2p^4$ for O. For both minima and the TS, both lattice constants and atomic positions were fully optimized until the maximal stress component is below 0.1 GPa and the maximal force component below 0.001 eV/Å. The Monkhorst-Pack k-point meshes up to (8×8×8) in Brillouin zone were utilized in order to obtain absolute energy convergence $<$ 0.5 meV/f.u at PBE functional level.

Accuracy on the energetics of pathways using different DFT functionals

In order to check the effect of the DFT functionals on the barrier of phase transition, we have also performed the hybrid DFT calculations using HSE06 functional[37]. The data is presented in Table SII, which compares the energetics of the key states using two different functionals (PBE and HSE06) at incrementing k-point mesh.

Our results in Table SII show that the relative energetics are converged for **k**-point mesh above 4x4x4 mesh for the 12-atom supercell. The hybrid HSE06 functional tends to reduce the energy difference of the states with respect to the m-phase. The energy difference between t- and m-phase is 101.0 meV/f.u. in HSE06 and increases to 110.7 meV/f.u in PBE, the difference being 9.7 meV. We would like to emphasize that the 0.01 eV/f.u. energy difference in the absolute energy difference is in fact quite small by itself considering different functionals utilized.

More importantly, for the concerned reaction pathways in this work, we found that both functionals lead to the identical energetic trend: (i) the TS1 and TS2 are energetically degenerate with the energy difference within 1 meV; (ii) the energy sequences are the same, i.e. TS3 < TS1~TS2 < TS4. This indicates that **Path III** is always less favorable at 0 GPa condition and thus Type-B OR is a minority reaction channel compared to Type-C OR; (iii) the o-phase is a trapping state at the low temperature due to much high barrier of o-m transition (96.4-66.3=30.1 from PBE; and 105.2-58.1=47.1 from HSE06) compared to t-o transition (114.1-110.7=3.4 from PBE and 111.7-101.0=10.7 from HSE06). From these comparisons in different functionals, we conclude that the mechanism of phase transition is not unchanged by DFT functionals.

According to the experimental value for the t-m phase transition temperature, e.g. ~1480 K[38] and ~1550 K[39] and our free energy calculations (by adding ZPE and entropy contribution), we can deduce that HSE06 functional predicts the t-m phase transition temperature is about 1450 K, which is slightly lower than the low-limit of experimental values, while PBE functional predicts 1580 K (see Figure 3 in text), which is slightly higher than high-limit of experimental values. Based on this fact and the same trend produced from functionals, we conclude that both functionals are acceptable at the current accuracy of quantum mechanical calculations.

It should be mentioned that GGA type (e.g. PBE) functional has been widely utilized for the prediction of the properties of ZrO_2. It remains unclear whether the hybrid functional can indeed perform better systematically than GGA (PW91 or PBE) or even LDA for all properties. Some recent representative publications utilizing GGA/LDA functionals for computing the properties of ZrO_2 can be found in references[40-45], where extensive experimental data has been compared with DFT results, showing DFT functionals are generally reliable for describing ZrO_2.

c. Phonon and free energy calculation

The phonon frequencies of the transition states were determined based on the density functional perturbation theory (DFPT)[46], employing the PHONOPY package [47]. For that, the size of the system was increased to (2×2×2) supercell (96-atom supercell) with the (2×2×2) Monkhorst-Pack mesh. With a displacement of ±0.01 Å of nonequivalent atoms, a set of displaced supercells was generated. For each 12-atom transition state, the number of displaced supercells is 72 (=12×6). For each displaced supercell, the DFPT/DFT calculations were performed to obtain the force on each atom due to the displacements. These forces were carried back to the PHONOPY to calculate the phonon dispersion curves. Helmholtz free energy (F), entropy of vibration (S_{vib}), and zero-point energy (ZPE) at finite temperature can be obtained from phonon spectra based on quasiharmonic approximation.

At a given temperature the lowest value of the free energy determines the stable phase. The free energy of the crystal is a sum of a ground state energy and the free energy contribution from the lattice vibrations. The first term is directly obtained from DFT calculation, i.e. at T=0 K. The second one is temperature dependent and in the harmonic approximation it is calculated from the phonon density of states using the following

equation,

$$F_{\text{harm}} = rk_B T \int_0^{\infty} g(\varpi) \ln[2\sinh(\frac{\hbar\varpi}{2k_B T})] d\varpi$$

where r is the number of degree of freedom in a primitive unit cell, ω denotes the phonon frequency, g(ω) denotes the density of phonon states (DOS), $\hbar$ is the Planck constant, and k_B is the Boltzmann constant. In this approach the thermal expansion of crystal is neglected.

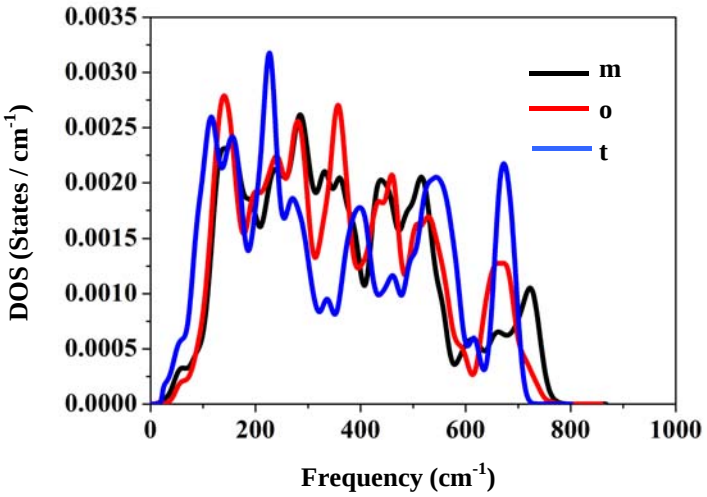

FIG. S4. The phonon densities of states of mono (m), ortho (o) and tetra (t) phase zirconia. Black: m-phase; Red: o-phase; Blue: t-phase. It shows that t-phase has a significant higher density of soft phonon density compared to m-phase, which explains that t-phase becomes more stable at high temperatures (see Figure 3 in text). The intermediate o-phase shows a higher soft phonon density than m-phase but less than t-phase.

d. Methods to determine the OR and search for atomic habit planes (coherent interface)

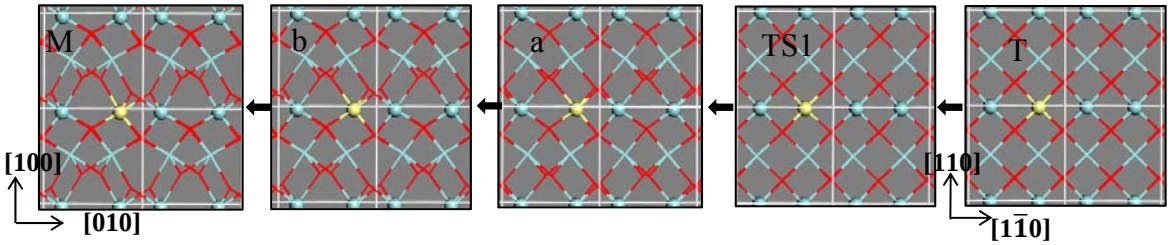

FIG S5. Snapshots from t-m transformation in **Path I** (the labeling of the states also see Fig. S3 profile). All are viewed down from $[001]_m$ and $[001]_t$. Zr atom: Cyan or yellow; O atom: Red. The yellow atoms highlights an atomic row with zero atomic movement at $[100]_m$.

The SSW pathway sampling provides the lowest energy pathway between two connecting phases, which determines the lattice and atom correspondence, as illustrate in Figure S5 for t-m phase transition in **Path I**. The lattice parameters and atomic coordinates of **Path I** utilized in the following analysis are provided in section **Part 4** Table **SII**. Note that the lattice and atom coordinates identified in the lowest pathways are generally not in conventional Bravais lattice of crystal. In the following, we describe in detail the three steps that are required to identify the atomic habit plane (coherent interface) between two phases.

Step1: Determine Strain Invariant Planes

Based on the lattice correspondence, we can first use the classical phenomenological theory of Martensitic crystallography (PTMC) [5, 48-53] to determine the invariant line strain, the possible habit planes and ORs.

Determine the principal axes of the phase transformation.

Let define two lattices as **T** and **M,** both (3x3) matrix of lattice.

A deformation gradient **F** matrix transform an initial lattice **T** to a final lattice **M**, as

$$\mathbf{FT= RBT=M}$$

$$\mathbf{F=RB}$$

where R is a rigid-body rotation matrix and B is a lattice deformation matrix, representing the generalized Bain deformation. In PTMC, **F** is also known as a homogeneous *invariant line strain*.

The Gauchy-Green deformation tensor is

$$\mathbf{C=F^TF=(T^T)^{-1}\,M^T\,MT^{-1}}$$

C is rotational invariant.

The principal axes are the eigenvectors ($\mathbf{e_i}$, i=1,2,3) of the Gauchy-Green deformation tensor

$$\mathbf{Ce_i= l_ie_i}$$

The strain energy of the lattice deformation is defined the sum of three eigenvalues, $\mathbf{l_i}$

$$I=\mathrm{tr}(\mathbf{F^TF})=\mathbf{l_1+\,l_2+l_3}$$

Take **Path I** in t-m phase transition as the example, three principal axes (Cartesian coordinate) are as follow using m-phase as initial phase and t-phase as final phase:

$\mathbf{e_1}$**:**	(0.0099	0.7755	$0.6313)_m$;	$\mathbf{l_1}$=0.82961
$\mathbf{e_2}$**:**	(0.9999	-0.0053	$-0.0093)_m$;	$\mathbf{l_2}$=0.95253
$\mathbf{e_3}$**:**	(0.0039	-0.6313	$0.7755)_m$;	$\mathbf{l_3}$=1.16559

Obviously, $\mathbf{e_2}$ direction is the principal axes with the lowest strain.

Determine the strain invariant lines (SIL) and strain invariant planes (SIP)

For Martensitic phase transition, three eigenvalues of matrix **C** could not be all larger than one or all smaller than 1 and in general $\mathbf{l_2}$ should be quite close to unity:

$$\mathbf{l_1 < 1;\ l_2 > 1;\ l_3 > 1;\quad or\quad l_1 < 1;\ l_2 < 1;\ l_3 > 1\quad (l_3 > l_2 > l_1)}$$

Using three eigenvectors **e** as the basis, we need to determine the strain invariant lines on a corn surrounding the maximum or the smallest $\mathbf{e_i}$. This is equivalent to find the fractional coordinate (*a,b,c*) in the following two equations.

$$a^2+b^2+c^2=1$$

$$a^2\,\mathbf{l_1}+b^2\,\mathbf{l_2}+c^2\,\mathbf{l_3}=1$$

While there are in principle infinite number of solutions for (*a,b,c*), the problem can be simplified by identifying the strain invariant lines on the plane defined by the largest and the smallest eigenvectors, $\mathbf{e}_1$ and $\mathbf{e}_3$., i.e. by setting

$$b=0$$

These strain invariant lines can thus be solved as

$$\boldsymbol{sil_1}=a\mathbf{e_1}+c\mathbf{e_3}\ \text{and}\ \boldsymbol{sil_2}=a\mathbf{e_1}-c\mathbf{e_3}$$

In **Path I** of t-m phase transition, two solutions of ***sil*** (Cartesian coordinate) vector on the plane with $\mathbf{e_1}\times\mathbf{e_3}$ normal are yielded:

sil1**:**	(0.0097	0.0949	$0.9954)_m$
sil2**:**	(-0.0042	-0.9940	$0.1091)_m$

Using a ***sil*** vector and another untilted line, e.g. the principal axes **e** normal to ***sil***, it is possible to construct the so-called strain invariant (minimum) plane, the habit plane. All lines on habit plane are unrotated, which should contain a strain invariant line and also an untilted line. These lines and their angle are unchanged under the rigid-body rotation and the lattice deformation. The habit plane normal ***sip***, a unit vector, can be solved using

$$\boldsymbol{sip_k}=\boldsymbol{sil_i}\times\mathbf{e_j}$$

$$\mathbf{F}\,\boldsymbol{sip_k}=\mathbf{RB}\,\boldsymbol{sip_k}=\boldsymbol{sip_k}$$

In **Path I** of t-m phase transition, two solutions of $\boldsymbol{sip_i}$, i=1, 2 with the minimum strain are yielded. In the convention of Miller plane, ***sip*** are named using (hkl) with real numbers:

***sip1*:**	(0.023	5.3798	$0.3834)_m$	$\boldsymbol{sip_1 = sil_1 \times e_2}$
***sip2*:**	(0.052	0.589	$5.210)_m$	$\boldsymbol{sip_2 = sil_2 \times e_2}$

Step 2: Determine the crystal planes with minimum strain and minimum atomic movement

Now we need to go beyond PTMC by considering the atomic movement in the phase transition.

The possible $\boldsymbol{sip_i}$ only takes into account the lattice strain between two connecting phases but the atomic match at the interface cannot be quantitatively measured. For diffusionless Martensitic phase transition, it is important that the atoms at the phase junction are closely matched and thus the atomic displacement needs to be as small as possible from one phase to another.

Based on the atom correspondence from the pathway obtained from SSW, we can search for the crystal plane with minimum strain and minimum atomic movement.

a. The minimum strain condition is first utilized to screen the possible crystal Miller planes by minimizing the dihedral angle between the crystal plane ((hkl) with integer number) and the $\boldsymbol{sip_i}$.
b. The atomic movement can be calculated by summing the displacement of each atom from initial to the final phase while projecting out those due to rigid-body rotation.

The atomic movement is composed of two types of movement, parallel to the crystal plane (hkl) and perpendicular to the plane. For Martensitic phase transition, the phase transition is achieved often via slipping or twinning and thus the atomic movement needs to be dominated by those parallel to the habit plane.

In **Path I** of t-m phase transition, if limiting the search within low index planes (hkl) with the absolute value of h, k, l being 0 or 1. Two solutions are yielded:

SOLUTION 1: $(010)_m$ plane, which is 4.22 degrees off ***sip1***. The atomic movement is 4.75 Å parallel to the plane and 3.61 Å perpendicular to the plane.
By switching to the notation in conventional Bravais lattice, $(010)_m$ is $\boldsymbol{(001)_m}$

SOLUTION 2: $(001)_m$ plane, which is 6.29 degrees off ***sip2***. The atomic movement is 5.10 Å parallel to the plane and 2.94 Å perpendicular to the plane.
By switching to the notation in conventional Bravais lattice, $(001)_m$ is $\boldsymbol{(100)_m}$

$\boldsymbol{(100)_m}$ has the smallest atomic movement (2.94 Å) perpendicular to the plane.

Step 3: Identify the atomic habit plane (interface)

Finally, we utilize the determined possible atomic habit planes to establish the interface between two phases. An atomic habit plane needs to exhibit a coherent interface between two phases, i.e. with the lowest interfacial energy.

For **Path I** in t-m phase transition, we have two likely interfaces as suggested from **Step 2**: $\boldsymbol{(001)_m//(001)_t}$, and $\boldsymbol{(100)_m//(110)_t}$ (different OR). By manually joining the two surfaces of the two phase together, we found that $\boldsymbol{(100)_m}$ and $\boldsymbol{(110)_t}$ pair can form a coherent interface between the two phases. The as-established interface is shown in the Figure **S5**. We therefore conclude that $\boldsymbol{(100)_m//(110)_t}$ is the atomic habit plane and the overall OR can be written as $(100)_m//(110)_t$; $[001]_m//[001]_t$.

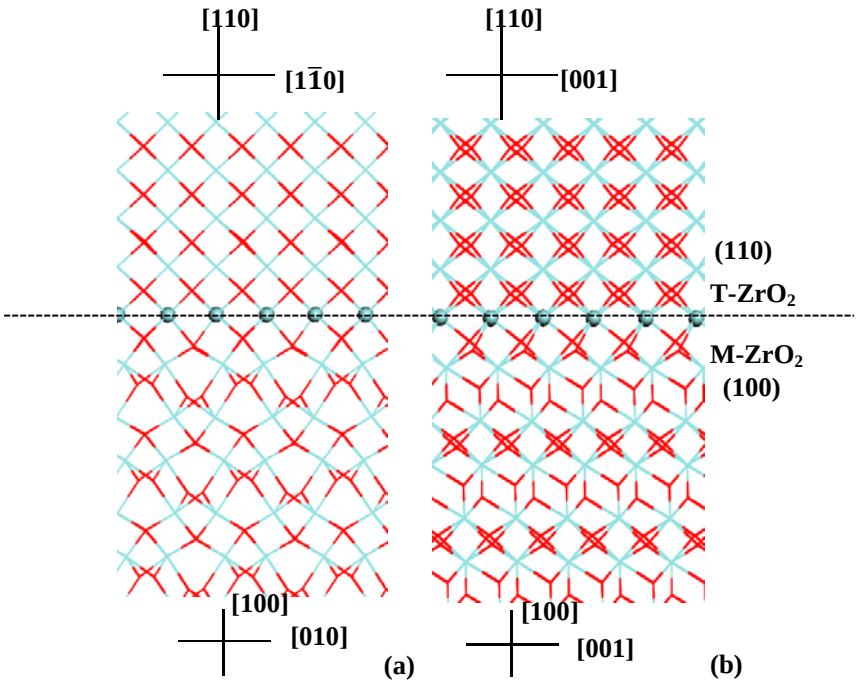

FIG. S6 Models of the t-m interfaces based on $(100)_m//(110)_t$; $[001]_m//[001]_t$ from two side views. Zr atom: Cyan; O atom: Red.

TABLE SIII. The OR and atomic habit planes (HP) for **Path II** (the structure of the crystals are listed in Part 4). The **e**, **I** and ***sil*** are as defined in Part 2d.

Path II (m-t)	m-o	o-t
$\mathbf{e}_1$	$(-0.7673, -0.0006, 0.6413)_m$	$(0.1367,-0.1416,-0.9804)_o$
$\mathbf{e}_2$	$(0.0001, -1, -0.0008)_m$	$(0.9891,0.075,0.127)_o$
$\mathbf{e}_3$	$(0.6413, -0.0006, 0.7673)_m$	$(0.0555,-0.9871,0.1503)_o$
$\mathbf{I}_1$	0.83641	0.98078
$\mathbf{I}_2$	0.94471	0.99911
$\mathbf{I}_3$	1.17518	1.01015
$\boldsymbol{sil}_1$	$(-0.1061, -0.0008, 0.9944)_m$	$(0.1253,-0.8818,-0.4547)_o$
$\boldsymbol{sil}_2$	$(-0.9974,0.000,-0.072)_m$	$(-0.0354,-0.7154,0.6979)_o$
Atomic HP	$(100)_m//(001)_o$	$(110)_o//(1\bar{1}2)_t$
OR	$(100)_m//(110)_t$; $[001]_m//[001]_t$	

TABLE SIV The OR and atomic habit plane (HP) for **Path III** (the structure of the crystals are listed in Part 4). The **e**, **I** and ***sil*** are as defined Part 2d.

Path III (t-t')	t-t'
$\mathbf{e_1}$	$(0.0053,-1,0.001)_t$
$\mathbf{e_2}$	$(0.9991,0.0053,-0.0416)_t$
$\mathbf{e_3}$	$(0.0416,0.0012,0.9991)_t$
$\mathbf{I_1}$	0.94374
$\mathbf{I_2}$	0.99986
$\mathbf{I_3}$	1.05902
$\boldsymbol{sil}_1$	$(0.0329,-0.7147,0.6987)_t$
$\boldsymbol{sil}_2$	$(-0.0253,-0.7164,-0.6972)_t$
Atomic HP	$(1\bar{1}2)_t//(\bar{1}12)_{t'}$
OR	$(110)_t//(110)_{t'}$; $[001]_t//[1\bar{1}0]_{t'}$

References

(1) Bailey, J. E., *Proc. R. Soc. Lond. A* **1964,** *279*, 395-412.

(2) Wolten, G. M., *Acta Cryst.* **1964,** *17*, 763-765.

(3) Smith, D. K.; Newkirk, W., *Acta Cryst.* **1965,** *18*, 983-991.

(4) Patil, R. N.; Subbarao, E. C., *Acta Cryst. A* **1970,** *26*, 535-541.

(5) Bansal, G. K.; Heuer, A. H., *Acta Metall* **1974,** *22*, 409-417.

(6) Buljan, S. T.; McKinstry, H. A.; Stubican, V. S., *J. Am. Ceram. Soc* **1976,** *59*, 351-354.

(7) Muddle, B. C.; Hannink, R. H. J., *J.Am.Ceram.Soc* **1986,** *69*, 547-555.

(8) Chien, F. R.; Ubic, F. J.; Prakash, V.; Heuer, A. H., *Acta Mater.* **1988,** *46*, 2151-2172.

(9) Hayakawa, M.; Kuatani, N.; Oka, M., *Acta Metall* **1989,** *37*, 2223-2228.

(10) Hugo, G. R.; Muddle, B. C., *Mater.Sci.Forum* **1990,** *56-58*, 357-362.

(11) Zhu, W. Z.; Lei, T. C.; Zhou, Y.; Ding, Z. S., *J.Mater.Sci.Lett* **1996,** *15*, 69-71.

(12) Shevchenko, V. Y.; Madison, A. E.; Glushkova, V. B., *Glass Phys. Chem* **2001,** *27*, 400-405.

(13) Shevchenko, V. Y.; Khasanov, O. L.; Madison, A. E.; Lee, J. Y., *Glass Phys. Chem* **2002,** *28*, 322-325.

(14) Kasatkina, I.; Girgdiesa, F.; Resslera, T.; Carusoc, R. A.; Schattkac, J. H.; Urbana, J.; K.Weissa, *J.Mater.Sci* **2004,** *39*, 2151-2157.

(15) Wu, Y.-C.; Chiang, Y.-T., *J. Am. Ceram. Soc* **2011,** *94*, 2200-2212.

(16) Chiao, Y.-H.; Chen, I.-W., *Acta metall* **1990,** *38*, 1163-1174.

(17) Simeone, D.; Baldinozzi, G.; Gosset, D.; Dutheil, M.; Bulou, A.; Hansen, T., *Phys.Rev. B* **2003,** *67*, 064111-064118.

(18) Trolliard, G.; Mercurio, D.; Perez-Mato, J. M., *Z.Kristallogr.* **2011,** *226*, 264-290.

(19) Liu, S.; Hu, W.; Zhang, Y.; Xiang, J.; Wen, F.; Xu, B.; He, J.; Yu, D.; Tian, Y.; Liu, Z., *J.Appl.Cryst* **2014,** *47*, 684-691.

(20) Shang, C.; Liu, Z. P., *J.Chem.Theory Comput* **2013,** *9*, 1838-1845.

(21) Zhang, X. J.; Shang, C.; Liu, Z. P., *J.Chem.Theory Comput* **2013,** *9*, 3252-3260.
(22) Shang, C.; Zhang, X. J.; Liu, Z. P., *Phys. Chem. Chem. Phys.* **2014,** *16*, 17845-17856.
(23) Zhang, X.-J.; Shang, C.; Liu, Z.-P., *J.Chem.Theory Comput* **2013,** *9*, 5745-5753.
(24) Shang, C.; Liu, Z. P., *J Chem Theory Comput* **2012,** *8*, 2215-2222.
(25) Shang, C.; Liu, Z.-P., *J Chem Theory Comput* **2010,** *6*, 1136-1144.
(26) Trinkle, D.; Hennig, R.; Srinivasan, S.; Hatch, D.; Jones, M.; Stokes, H.; Albers, R.; Wilkins, J., *Physical Review Letters* **2003,** *91*, 025701-025704.
(27) Osamu Ohtaka; Takamitsu Yamanaka; Shoichi Kume; Naoki Hara; Hajime Asano; Izumi, F., *Proc. Japan Acad.* **1990,** *66*, 193-196.
(28) Kisi, E. H.; Howard, C. J., *Key Engineering Materials* **1998,** *153-154*, 1-36.
(29) Trolliard, G.; Benmechta, R.; Mercurio, D., *Acta Materialia* **2007,** *55*, 6011-6018.
(30) Yu, J.; Devanathan, R.; Weber, W. J., *J. Mater. Chem* **2009,** *19*, 3923–3930.
(31) Soler, J. M. A., E.; Gale, J. D.; Garcia, A.; Junquera, J.; Ordejon, P.; Sanchez-Portal, D., *J. Phys.: Condens. Matter* **2002,** *14*, 2745-2779.
(32) Anglada, E.; M. Soler, J.; Junquera, J.; Artacho, E., *Physical Review B* **2002,** *66*, 205101.
(33) John P. Perdew; Kieron Burke; Ernzerhof, M., *Phys.Rev.Lett* **1996,** *77*, 3865-3868.
(34) Kresse, G.; Furthmüller, J., *Phys.Rev. B* **1996,** *54*, 11169-11186.
(35) Kresse, G.; Furthmüller, J., *Comput.Mater.Sci* **1996,** *6*, 15-50.
(36) Blöchl, P. E., *Phys.Rev. B* **1994,** *50*, 17953-17979.
(37) Krukau, A. V.; Vydrov, O. A.; Izmaylov, A. F.; Scuseria, G. E., *J. Chem. Phys.* **2006,** *125*, 224106-224111.
(38) Ackermann, R. J.; Raum, E. G.; Alexander, A., *High Temp. Sci.* **1975,** *7*, 304-316.
(39) Frey, F.; Boysen, H.; Vogt, T., *Acta Cryst.B* **1990,** *46*, 724-730.
(40) Luo, X.; Zhou, W.; Ushakov, S.; Navrotsky, A.; Demkov, A., *Phys.Rev. B* **2009,** *80*, 134119-134132.
(41) Sternik, M.; Parlinski, K., *J. Chem. Phys.* **2005,** *122*, 064707-064713.
(42) Kuwabara, A.; Tohei, T.; Yamamoto, T.; Tanaka, I., *Physical Review B* **2005,** *71*, 064301-064307.
(43) Al-Khatatbeh, Y.; Lee, K. K. M.; Kiefer, B., *Physical Review B* **2010,** *81*, 214102-214112.
(44) Zhu, W.; Wang, R.; Shu, G.; Wu, P.; Xiao, H., *Structural Chemistry* **2011,** *23*, 601-611.
(45) McKenna, K. P.; Wolf, M. J.; Shluger, A. L.; Lany, S.; Zunger, A., *Phys. Rev. Lett* **2012,** *108*, 116403-116408.
(46) Baroni, S.; Gironcoli, S. d.; Corso, A. D., *Rev. Mod. Phys.* **2001,** *73*, 515-561.
(47) Togo, A.; Oba, F.; Tanaka, I., *Phys.Rev. B* **2008,** *78*, 134106-134114.
(48) Bowles, J. S.; Mackenzie, J. K., *Acta Metall* **1954,** *2*, 129-137.
(49) Mackenzie, J. K.; Bowles, J. S., *Acta Metall* **1954,** *2*, 138-147.
(50) M.S.Wechsler; T.A.Lieberman, *Trans.Am.Inst.Min.Engrs* **1953,** *197*, 1503-1515.
(51) Wayman, C. M., *New York:Macmillan Co.* **1964**, 76-80.
(52) Wayman, C. M., *J. Less-Common Metals* **1972,** *28*, 97-105.
(53) Xiao, X. L.; Luo, C. P.; liu, J. W., *Sci. China, Ser. E* **2002,** *45*, 58-64.

Part 3 Variation of the coordination number of Zr ions in phase transition

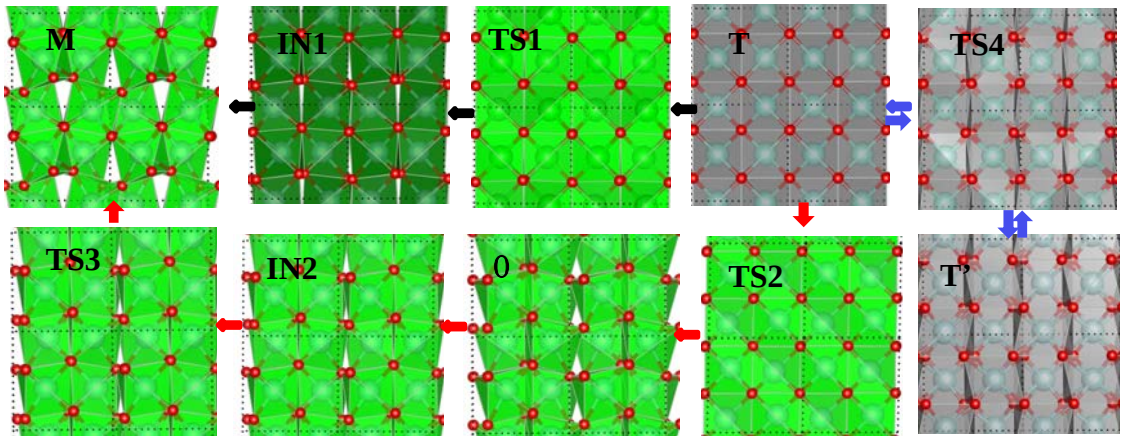

FIG.S7. Polyhedron structure snapshots from monoclinic to tetragonal in three lowest energy pathways. All are viewed down from $[001]_m$ and $[001]_t$. IN1 and IN2 are representative intermediate states along the pathway. Polyhedrons are colored according to the coordination number of Zr ions. Green: 6-coordinated; Lime: 7-coordinated; Grey: 8-coordinated..

Part 4 The Cartesian atomic coordinates for key states in Path I, II and III

Path I

t-phase		a= 5.154 b=5.304 c=5.154 α=β=γ=90°	
	X	Y	Z
O	3.8033376	2.473369801	0.651351652
O	3.813085	2.430910363	3.303471903
O	3.8118187	5.007707002	3.888530593
O	3.8039373	5.04945882	1.235934795
O	1.227537	5.052320073	0.652901003
O	1.233343	5.010753043	3.305035969
O	1.2250468	2.4731064	1.237269882
O	1.2359974	2.431977733	3.889847462
Zr	5.0710282	3.744594316	2.26900122
Zr	2.4935919	1.16865683	2.269985039
Zr	2.4990523	3.742816516	4.923647904
Zr	5.0764868	1.164934278	4.921571405
TS1		a=5.164 b=5.343 c=5.165 α=87° β=γ=90°	
	X	Y	Z
O	2.49476	0.888314	3.856278
O	2.481624	3.559507	3.85651
O	5.058454	4.118481	3.776015
O	5.080724	1.446569	3.7754
O	5.051086	0.685603	1.187979
O	-0.07044	3.356639	1.186819

O	2.532251	1.393949	1.288473
O	2.446112	4.065882	1.289282
Zr	3.864563	2.532475	5.077894
Zr	1.280656	2.477296	2.532467
Zr	3.694013	5.150465	2.536007
Zr	1.107952	5.204619	5.081344
m-phase		a=5.281 b=5.4042 c=5.2196 α=80^o β=γ=90^o	
	X	Y	Z
O	4.0482786	2.481702959	1.527028954
O	4.0483148	2.557072245	4.229065433
O	3.5388048	5.122356023	4.393263516
O	3.5388333	5.197357136	1.691077031
O	0.8760293	4.737957761	0.287617624
O	0.8759908	0.3011147	2.989614803
O	1.5652383	2.941622645	2.054538643
O	1.5653019	2.097174406	4.756675548
Zr	4.9445097	4.069602832	2.940528728
Zr	2.6422744	1.428989609	2.979805276
Zr	2.6427215	3.609602629	5.681883574
Zr	4.9448122	0.968645046	5.642518708
Path II t-o			
t-phase		a= 5.154 b=5.154 c=5.306 α=β=γ=90^o	
	X	Y	Z
O	3.835619	4.744989	3.930029
O	3.825117	2.174400	4.516754
O	1.249454	4.735006	1.863021
O	1.255660	4.748139	4.516119
O	1.253732	2.157062	1.278206
O	3.832621	2.161106	1.863691
O	3.825910	4.733772	1.277150
O	1.251272	2.169737	3.931065
Zr	2.548721	3.454047	2.897791
Zr	2.537699	0.868775	0.244093
Zr	-0.039366	3.446082	0.243973
Zr	-0.028015	0.876598	2.896105
TS2		a=5.163 b=5.158 c=5.325 α=β=γ=90^o	
	X	Y	Z
O	3.447216	4.261664	3.679989
O	3.535699	1.648276	4.303547
O	0.807147	4.058459	1.733838
O	0.865632	4.262950	4.387669
O	0.905661	1.517667	1.099615
O	3.486597	1.515709	1.645754
O	3.387233	4.055612	1.008683

O	0.954035	1.649722	3.766485
Zr	2.272826	2.886156	2.665879
Zr	2.258352	0.339889	-0.006779
Zr	-0.309055	2.885356	0.077707
Zr	-0.321391	0.341330	2.752823
o-phase		a=5.157 b=5.131 c=5.345 α=β=γ=90^{o}	
	X	Y	Z
O	3.468504	5.053412	3.641940
O	4.006533	2.327688	4.372743
O	0.892195	4.362254	2.201729
O	0.888347	5.054298	4.877569
O	1.432559	1.958282	1.467397
O	4.011018	1.956943	1.697600
O	3.472108	4.362918	0.967466
O	1.428070	2.326893	4.142044
Zr	2.734446	3.340325	2.757341
Zr	2.736254	0.942930	0.082616
Zr	0.156842	3.341685	0.408983
Zr	0.154661	0.941415	3.084030
Path II o-m			
o-phase		a=5.156 b=5.131 c=5.351 α=β=γ=90^{o}	
	X	Y	Z
O	2.082771	5.052031	2.966345
O	4.120521	2.325691	3.469187
O	4.662644	4.3592	1.528965
O	4.661203	5.05173	4.203812
O	1.543323	1.954216	1.025811
O	4.122238	1.954281	0.793644
O	2.083861	4.359708	0.291227
O	1.541573	2.326147	3.701238
Zr	2.817757	3.339865	2.083698
Zr	2.817407	0.941122	4.758931
Zr	0.238163	3.339911	5.087017
Zr	0.239013	0.941591	2.41144
TS3		a=5.190 b=5.156 c=5.452 α=90 ^{o} β=93 ^{o} γ=90^{o}	
	X	Y	Z
O	1.778949	4.975775	2.926216
O	3.889803	2.274251	3.377355
O	4.484212	4.503944	1.299968
O	4.306585	4.928757	4.019927
O	1.409848	2.130856	1.198866
O	4.067022	2.002178	0.657218
O	1.956134	4.458376	0.206383
O	1.232775	2.146547	3.918978

Zr	2.788739	3.471237	2.012364
Zr	2.611875	0.805957	4.732053
Zr	-0.09778	3.292485	5.083042
Zr	0.079478	0.984528	2.362621
m-phase		a=5.221 b=5.279 c=5.409 β=99.7° α=γ=90°	
	X	Y	Z
O	1.613478	5.256981	2.763659
O	3.50311	2.238702	3.44638
O	4.432458	4.878503	1.032055
O	3.976482	4.804828	3.697755
O	1.100607	2.61771	1.715169
O	3.95884	2.165782	0.780884
O	2.06973	4.425996	0.097809
O	0.644638	1.786285	4.380878
Zr	2.836085	3.752251	2.026826
Zr	2.380154	0.652147	4.692711
Zr	-0.57782	3.291568	5.117323
Zr	-0.12159	1.112951	2.451459
Path III t-t'			
t-phase		a=5.154 b=5.306 c=5.155 α=β=γ=90°	
	X	Y	Z
O	3.71505	0.063191	4.95914
O	1.136096	2.130973	4.963859
O	1.136128	4.783927	4.958209
O	3.71373	2.716036	4.963575
O	3.713115	4.782796	2.381503
O	1.134951	2.714821	2.385861
O	3.712977	2.129974	2.385979
O	1.136909	0.061887	2.380966
Zr	2.421893	1.096067	3.673476
Zr	4.998763	3.749557	3.672406
Zr	4.999164	1.096577	1.096006
Zr	2.421087	3.749231	1.094856
TS4		a=5.155 b=5.197 c=5.196 α=β=γ=90°	
	X	Y	Z
O	3.68433	-0.04639	5.172845
O	1.171088	2.21882	5.173395
O	1.170056	4.817384	4.838745
O	3.684824	2.551854	4.83815
O	3.683708	4.817066	2.575063
O	1.16918	2.552064	2.575391
O	3.682866	2.218533	2.240055
O	1.169784	-0.04622	2.240836
Zr	2.427025	1.086507	3.706791

Zr	5.004292	3.685202	3.706923
Zr	5.003567	1.085709	1.108943
Zr	2.426134	3.684326	1.10908
t'-phase		a= 5.154 b=5.154 c=5.304 α=β=γ=90^{o}	
	X	Y	Z
O	3.726569	-0.22313	5.397858
O	1.150023	2.351027	5.397608
O	1.148752	4.929424	4.81278
O	3.724572	2.355466	4.813418
O	3.720283	4.932053	2.74545
O	1.143128	2.357317	2.745187
O	3.717552	2.352863	2.161056
O	1.142186	-0.22121	2.160409
Zr	2.432799	1.07017	3.779099
Zr	5.009772	3.647315	3.779378
Zr	5.00267	1.061022	1.127067
Zr	2.425663	3.638179	1.126525